Journal of Geophysical Research: Space Physics

RESEARCH ARTICLE
10.1029/2018JA025638

Modeling the Dawn/Dusk Asymmetry of Field Line Resonances

Andrew N. Wright[1], **Tom Elsden**[1], **and Kazue Takahashi**[2]

[1]Department of Mathematics and Statistics, University of St Andrews, St Andrews, UK, [2]The Johns Hopkins University Applied Physics Laboratory, Laurel, MD, USA

Key Points:
- Simulations of a magnetospheric waveguide that is asymmetric about noon are presented
- Fast mode refraction causes asymmetries in compressional waves to develop, along with the FLRs they excite
- FLRs are excited with larger amplitude at dawn compared to dusk

Supporting Information:
- Movie S1
- Supporting Information S1

Correspondence to:
A. N. Wright,
anw@st-and.ac.uk

Citation:
Wright, A. N., Elsden, T., & Takahashi, K. (2018). Modeling the dawn/dusk asymmetry of field line resonances. *Journal of Geophysical Research: Space Physics*, *123*. https://doi.org/10.1029/2018JA025638

Received 2 MAY 2018
Accepted 28 JUN 2018
Accepted article online 5 JUL 2018

Abstract Field line resonances (FLRs) are observed to occur preferentially and have larger amplitudes at dawn compared to dusk. We present simulations of FLR excitation in a magnetospheric waveguide that can reproduce this behavior. Crucially, our equilibrium is asymmetric about noon. Even when this system is driven in a symmetric fashion about noon, the fast waves that are established in the magnetosphere develop asymmetries—as do the FLRs they excite. Fast mode ray trajectories are employed to show that the asymmetry evolves due to refraction. Preferential FLR excitation at dawn is further reinforced by calculating the Resonance Map. This shows that the Resonant Zone at dawn coincides with a large-amplitude coherent fast mode driver, which is not the case at dusk. These factors result in FLRs having a larger amplitude at dawn compared to dusk.

1. Introduction

The theory of ultralow frequency (ULF) toroidal Alfvén waves on closed field lines and their resonant excitation has a rich history spanning five decades (Chen and Hasegawa, 1974; Southwood, 1974). Originally, the theory was based upon 1-D normal mode models, which were extended to include time dependence (Allan et al., 1986; it ; Mann et al., 1995). Recognizing the importance of a dipolar-like equilibrium magnetic field, 2-D (axisymmetric) studies by Lee and Lysak (1989) and Wright and Thompson (1994) confirmed the persistence of resonant coupling more generally. With increasing computer power simulations we are now able to study excitation of field line resonances (FLRs) in 3-D (Claudepierre et al., 2010; Degeling et al., 2010; Ellington et al., 2016; Elsden & Wright, 2018).

The simulation work has recently provided enough clues of how the resonant coupling process occurs in 3-D that the formulation of an analytical theory has recently been advanced and corroborated by numerical solutions (Wright & Elsden, 2016). The 3-D resonant process is quite different from that in an axisymmetric 2-D model: In 2-D there is a unique resonant L shell surface, and the FLR polarization is exactly toroidal. In contrast, in 3-D there is not a unique resonant L shell, but a range of L shells that can potentially support FLR excitation in what is termed the Resonant Zone. Moreover, in 3-D the FLRs that are established are not toroidally polarized, and will occur on a surface that actually crosses L shells. In addition, there are an infinite number of such permissible resonant surfaces and there is not currently a complete understanding of which surfaces are favored in a given situation.

When trying to interpret observations from dawn, noon, and dusk, it is not possible to avoid the fact that the magnetosphere flares out on its flanks and has a plasma density that is asymmetric about noon (Fujita & Itonaga, 2003; Gallagher et al., 2000; Sandhu et al., 2017). Both these properties require us to adopt a 3-D model of FLR excitation. This will be particularly important when trying to understand observed differences between dawn and dusk. In the outer magnetosphere ($L > 6$), the most commonly observed ULF waves are Pc5 pulsations, which exhibit sinusoidal waveforms and have periods typically in the range 150–600 s. The pulsations are attributed to fundamental toroidal Alfvén waves, and the local time, and L dependence of their amplitude and polarization have been explained by the theory of field line resonance (e.g., Southwood, 1974). An interesting feature of Pc5 pulsations is that their occurrence is more frequent and amplitude is higher at dawn than at dusk. This feature has been observed both on the ground (Baker et al., 2003; Gupta, 1975) and in space (Kokubun, 2013; Nosé et al., 1995; Takahashi et al., 2016). Early theoretical studies attributed the asymmetry to the dawn/dusk asymmetry of the Kelvin-Helmholtz instability, which is expected from the dawn/dusk asymmetry of the magnetosheath magnetic field that results from interplanetary magnetic field following the Parker spiral (e.g., Lee & Olson, 1980). However, this mechanism does not appear to be effective because the

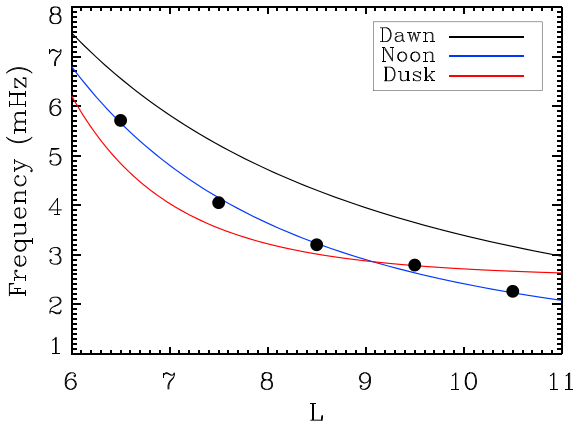

Figure 1. Variation of the fundamental toroidal Alfvén wave frequency at dawn, noon, and dusk. The black dots are median f_{T1} frequencies at noon found from analyzing THEMIS data as described in Takahashi et al. (2016). THEMIS = Time History of Events and Macroscale Interactions during Substorms.

same Pc5 asymmetry is found even when the interplanetary magnetic field orientation is ortho-Parker spiral (Takahashi et al., 2016).

Takahashi et al. (2016) interpreted the dawn/dusk asymmetry in FLR amplitude and detection rate in terms of the coupling efficiency as described in the 1-D (radial) model of Kivelson & Southwood (1986) (see their Figure 2, and Figure 9 of Takahashi et al., 2016). The coupling efficiency of the fast mode to an FLR depends fundamentally on the magnetic pressure gradient along the resonance, which can be thought of as analogous to the driving term of a harmonic oscillator (Wright & Thompson, 1994). The magnetic pressure gradient depends upon many factors such as wave numbers and the structure of the medium. In particular, Takahashi et al. (2016) noted that the different Alfvén speed (and associated Alfvén frequency) profiles found at dawn and dusk will mean that stronger coupling is expected at dawn.

The Alfvén speed variation, and in particular how it is different at dawn and dusk, is the key quantity in understanding why FLRs have different properties at dawn and dusk. This is most likely due to a systematic dawn/dusk asymmetry in plasma mass density associated with drainage plumes or the presence of low-energy O^+ ions in the afternoon. Although it is often difficult to measure these ions directly, their presence has been inferred from magnetosiesmology (Takahashi et al., 2008). Test particle results reported by Nosé et al. (2015) also show evidence of heavy ion accumulation in the afternoon and at dusk outside the plasmasphere. While there may be some dawn/dusk asymmetry of the geomagnetic field, there have not been any reports of a systematic asymmetry as significant as that of the heavy ions. Moreover, if the additional mass at dusk is due to low-energy heavy ions, they will contribute mass but not a significant pressure. Hence, we would not expect these ions to cause an asymmetry in the magnetic field.

Recently, the broadband excitation of a 3-D flaring waveguide has produced a clear picture of how FLRs can be excited when the system is symmetric about the noon meridian (Elsden & Wright, 2018). In this article we explore the hypothesis of Takahashi et al. (2016) within the context of a 3-D waveguide model in an effort to gain more insight into how factors such as fast mode propagation, refraction and dispersion affect FLR excitation in an asymmetric waveguide.

The paper is structured as follows: Section 2 describes the numerical model; section 3 presents results of FLR excitation; section 4 interprets properties of fast waveguide modes; and section 5 contains concluding remarks.

2. Model

2.1. Numerical Model

The simulation domain is based upon a 2-D dipole with a 3-D Alfvén speed variation and has been described elsewhere (Elsden & Wright, 2017; Wright & Elsden, 2016). A field-aligned coordinate system (α, β, γ) is employed for numerical efficiency: α labels L shells so plays the role of a radial-like coordinate; β is the azimuthal-like coordinate; and γ a field-aligned coordinate. In the simulations presented here, $0.5 < \alpha < 1.0$, $-2.25 < \beta < 2.25$, and $-0.525 < \gamma < 0.525$. In the equatorial plane α and β correspond to distance. For the

purposes of comparing with observations we map $0.5 < \alpha < 1.0$ to $6 < L < 11$, meaning $dL/d\alpha = 10$ and simulation lengths are normalized by 10 R_E. 12 MLT is at $\beta = 0$, and +ve/−ve β correspond to the dusk/dawn flanks. The equatorial plane corresponds to $\gamma = 0$, and on a central L shell ($\alpha = 0.75$) γ corresponds to distance along that specific field line. (See Wright & Elsden, 2016, for details of the scale factors and numerical grid.) The observed fundamental toroidal frequency/period at noon for $L = 6$ (the inner edge of our domain) are 6.80 mHz/147.1 s (see next section) and is used to normalize time. Hence, speeds are normalized by 10 R_E/147.1 s = 433.2 km/s.

The time-dependent, cold linear magnetohydrodynamic equations are formulated in this coordinate system, and we remove the possibility of resonant singularities by including a small amount of dissipation in the form of a linear drag coefficient $\nu = 0.1$ (see equations (9)–(13) of Elsden & Wright, 2017). The waveguide is excited in a similar fashion to that described in Elsden and Wright (2018): the magnetopause centered on noon experiences an increase in pressure, such as that associated with an increase in solar wind dynamic pressure. The linear magnetic pressure is Bb_γ/μ_o, where b_γ is the compressional (or field-aligned) magnetic field perturbation and B is the background magnetic field strength. Hence, imposing $b_\gamma \sim \sin^2(\pi t/\tau_d)\cos^2(\pi\beta/(2\ell_\beta))\cos(k_\gamma\gamma)$ on the magnetopause ($\alpha = 1$) when $0 < t < \tau_d$ and $-\ell_\beta < \beta < \ell_\beta$ ($b_\gamma = 0$, otherwise) gives a localized push for a duration of τ_d over an extent of $2\ell_\beta$ centered at noon. The wavenumber k_γ is chosen to give a fundamental dependence on γ. For the results presented here $\tau_d = \pi/2$ and $\ell_\beta = 1$.

The ionospheric boundaries have nodes of velocity and b_γ, and antinodes of the other fields, while the inner boundary (at $\alpha = 0.5$) has a node of the α components of velocity and magnetic field and antinodes of the other fields. The boundary condition at the ends of the β domain do not play a role, as we introduce buffer zones when $|\beta| > 2.0$ where ν is increased to 1. This has the effect of absorbing any waves that impinge on them, and so allows us to mimic antisunward propagation around the flanks and into the magnetotail. The simulation uses a grid size of $(301, 401, 51)$ points in (α, β, γ), and for a typical run energy continuity is met to one part in 10^4.

2.2. Alfvén Speed Profile

The Alfvén speed variation is chosen to match observations of the fundamental toroidal Alfvén frequency (f_{T1}) variation with L shell reported by Takahashi et al. (2016). They used THEMIS observations to determine the variation at 6 MLT and 18 MLT. The empirical formulas they derived for f_{T1} at dawn and dusk are plotted in Figure 1. The dawn/dusk asymmetry in f_{T1} (in which the value at dawn is always higher than the corresponding value at dusk) is also consistent with the results in Figure 2 of Sandhu et al. (2018) who used realistic magnetic field and plasma density to calculate the time-of-flight f_{T1}. In Figure 1 we also plot data (as dots) from the 12 MLT slice of Figure 7 in Takahashi et al. (2016). The blue line is a fit to the dots which has the form

$$f_{T1} = 0.9311 + 732.5L^{-2.694}\ \text{mHz}. \tag{1}$$

There is evidently considerable asymmetry. For example, at dusk a 3-mHz FLR would be found at $L \approx 8.5$, whereas at dawn it would be located at $L \approx 11$. The key step in our simulation is to define an Alfvén speed variation ($V_A(\alpha, \beta, \gamma)$) that reproduces these profiles at noon ($\beta = 0$), dawn, and dusk ($\beta = \pm 2.0$). To achieve this, we note the relation between α and L [i.e., $\alpha = (L - 1)/10$] can be used to determine the variation of f_{T1} with α at dawn, noon, and dusk. We then interpolate the variation with β to second order using

$$f_{T1}(\alpha, \beta) = a_0(\alpha) + a_1(\alpha)\beta + a_2(\alpha)\beta^2. \tag{2}$$

The dawn, noon, and dusk frequencies (at a given L, or equivalently α) are used to determine the quadratic coefficients $a_0(\alpha)$, $a_1(\alpha)$, and $a_2(\alpha)$. The resulting function will match the profiles shown in Figure 1 and vary smoothly between them.

With $f_{T1}(\alpha, \beta)$ known, we can determine $V_A(\alpha, \beta, \gamma)$ that is consistent with these frequencies. There is some arbitrariness regarding the field-aligned variation of V_A since two different profiles could yield the same value of f_{T1} on the same field line. For numerical efficiency (related to the CFL condition (de Moura & Kubrusly, 2013)) we take V_A to be constant along any given field line, but vary from one field line to another. Hence, we need to determine the function $V_A(\alpha, \beta)$ and assign it so that the natural frequencies match those given by $f_{T1}(\alpha, \beta)$. This was achieved by initially setting $V_A = 1$ and shooting for the fundamental toroidal frequency (Wright & Elsden, 2016) to get the value $f_{T1}(\alpha, \beta, V_A = 1)$. The V_A required to produce observed frequency of $f_{T1}(\alpha, \beta)$

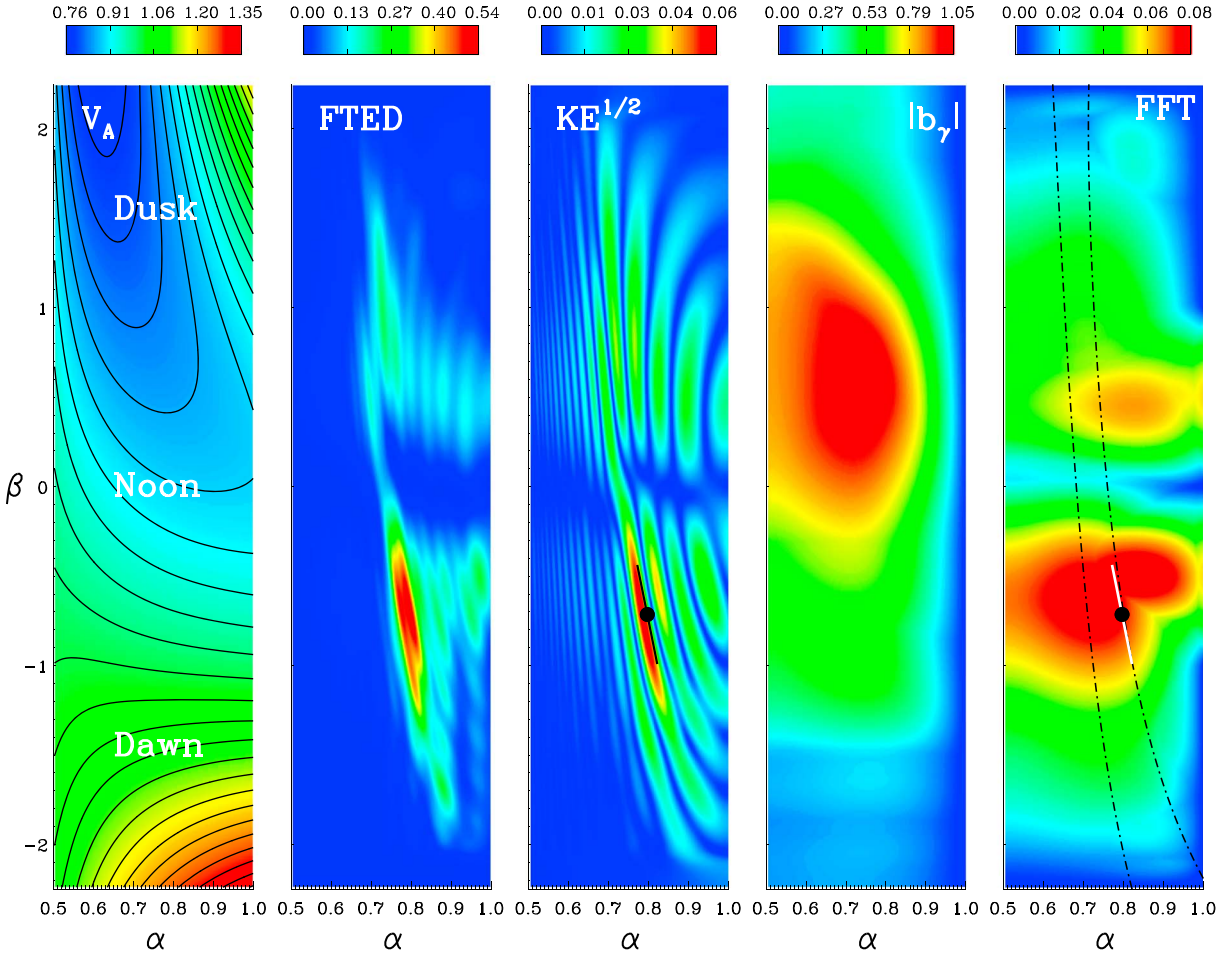

Figure 2. The variation of key quantities in the equatorial plane: From left to right, (first panel) V_A profile; (second panel) FTED; (third panel) square root of kinetic energy density (the dot is the location of the FTED maximum, and the line indicates the polarization of the Alfvén waves); (fourth panel) $\int |b_\gamma(\alpha, \beta, 0, t)|dt$ for $5.4 < t < 9.6$; (fifth panel) Contours of FFT of $(\nabla b_\gamma)_\beta$. Overplotted are the toroidal (right) and poloidal (left) boundaries of the Resonant Zone. The white line indicates the Alfvén wave polarization (also shown in the third panel as the black line). FTED = Flux Tube Energy Density; FFT = fast Fourier transform.

is $V_A(\alpha, \beta) = f_{T1}(\alpha, \beta)/f_{T1}(\alpha, \beta, V_A = 1)$. This process was repeated for all (α, β) grid points, and the resulting $V_A(\alpha, \beta)$ is shown as the first panel in Figure 2.

The simulation was run as described above to a time of $t = 21.41$. (A movie of key quantities is available as supporting information Movie S1.) The results are discussed in the following sections.

3. Field Line Resonances

3.1. FLR Location and Polarization Angle

Elsden and Wright (2017) show how the energy density integrated along an elemental flux tube can be used to define the Flux Tube Energy Density (FTED). It corresponds to the energy contained in a flux tube of unit area in the equatorial plane, and a contour plot of FTED can be used to infer the location of FLRs. The second panel in Figure 2 shows FTED at $t = 21.410$, and the peaks at dawn ($\alpha = 0.797$, $\beta = -0.714$) and dusk ($\alpha = 0.728$, $\beta = 0.934$) are evident. There is clearly a smaller amplitude at dusk. Structure within the resonance can be studied using a contour plot of kinetic energy density (or its square root) as shown in the third panel of Figure 2 at $t = 13.916$. This reveals phase-mixing ridges whose phase motion runs toward lower Alfvén frequency, that is, toward the magnetopause.

The results in this simulation can be contrasted with those of Elsden and Wright (2018) where the waveguide and magnetopause driving were both symmetric about noon. All of their plots for Alfvén and fast modes showed the expected perfect symmetry about noon. Although the present simulation has a driver that is symmetric about noon, the asymmetric V_A has caused obvious asymmetries in the Alfvén waves—as seen

in the second and third panels of Figure 2. Since the Alfvén waves are driven by the fast mode we would anticipate that the fast mode in the current simulation is also asymmetric about noon.

This conjecture can be checked by using the compressional magnetic field in the equatorial plane, $b_\gamma(\alpha, \beta, 0, t)$ as a signature of the fast mode. The fast mode will propagate such that asymmetric features become increasingly obvious as time passes. With this in mind we consider the interval $t > 5$ to avoid the period immediately following the symmetric driving. The fast mode will have a complicated spatial structure that varies with time which we do not wish to analyze here. Rather, we simply want to know where the fast mode is concentrated, and whether it possesses any asymmetry. For our purposes considering $\int |b_\gamma(\alpha, \beta, 0, t)|\mathrm{d}t$ for $5.4 < t < 9.6$ will suffice and is shown as the fourth panel in Figure 2. This is clearly asymmetric (in contrast with Figure 9 of Elsden & Wright, 2018) and is consistent with an asymmetric Alfvén wave response. The propagation of the fast mode will be studied in greater detail in the following section.

For the moment we return to properties of the phase-mixed Alfvén waves shown in the third panel of Figure 2. The black dot plotted in this panel corresponds to the dawn FTED peak ($\alpha = 0.797$, $\beta = -0.714$), and the line through it was drawn to lie parallel to the ridges. Wright and Elsden (2016) showed that the magnetic field, plasma displacement ($\boldsymbol{\xi}$), and velocity perturbations ($\mathbf{u} = \partial\boldsymbol{\xi}/\partial t$) of the Alfvén wave are also aligned with the ridges in this plot, so measuring the angle of this line to the β axis provides the polarization of the Alfvén wave here ($\theta = 0.09$ rad). Building on the general Alfvén wave eigenfrequency equation of Singer et al. (1981), Wright and Elsden (2016) showed how it could be adapted for Alfvén waves of any polarization angle,

$$\frac{\partial}{\partial\gamma}\left(\frac{h_{\beta'}}{h_{\alpha'}h_\gamma}\frac{\partial}{\partial\gamma}(\xi_{\beta' n}h_{\alpha'}B)\right) + \omega_{An}^2 h_{\beta'}h_\gamma\frac{B}{V_A^2}\xi_{\beta' n} = 0. \tag{3}$$

Here (α', β') are rotated coordinates such that the unit vector $\mathbf{e}_{\beta'}$ is aligned with the Alfvén wave fields and makes an angle θ to $\mathbf{e}_\beta$, and $\xi_{\beta' n}$ is the nth Alfvén wave eigenfunction with eigenfrequency ω_{An}. Once the scale factors have been determined for the field-aligned coordinates (α, β, γ), equations (20) and (22) of Wright and Elsden (2016) show how the scale factors $h_{\alpha'}$ and $h_{\beta'}$ can be evaluated. Such a calculation gives an Alfvén frequency for the dawn peak of $\omega_A = 2.914$ for the observed polarization angle ($\theta = 0.09$) at the dawn FTED peak ($\alpha = 0.797$, $\beta = -0.714$).

It is important to note that the FLRs in Figure 2 do not have a toroidal polarization angle ($\theta = 0$), but have $\theta = 0.09$. This means that they have a polarization angle that is intermediate between the toroidal and the poloidal Alfvén modes. It is also evident that these FLRs actually *cross L* shells — something that toroidal Alfvén waves will not do.

3.2. FLR Driver

To understand how the asymmetric FLRs are driven, it is necessary to study the fast waveguide mode which drives them. The frequency of this mode can be studied by considering $b_\gamma(t)$ for several points down the center of the waveguide and is shown in the left-hand panel of Figure 3 for $(\alpha, \beta) = (0.75, -1)$, (0.75,0), (0.75,0.5), and (0.75,1). The right-hand panel shows that the corresponding frequency spectra have a common waveguide frequency of $f_{wg} = 0.46$, confirming that the fast wave does indeed have a global nature. The peak FLR frequency found using the polarization $\theta = 0.09$ and equation (3) for the fundamental ($n = 1$) eigenmode was $\omega_A = 2.914$ corresponding to $f_A = \omega_A/2\pi = 0.464$, confirming that the largest amplitude Alfvén waves are indeed resonantly driven.

The drift of the fast mode to dusk ($\beta > 0$) seen in the fourth panel of Figure 2 will obviously produce some asymmetry in the FLRs that it excites; however, it is not clear from this panel alone where FLRs will be excited preferentially. To gain some insight into this question, we need to recognize that it is not b_γ that drives FLRs but the magnetic pressure gradient: specifically, the component of this gradient aligned with the FLR ridges in the third panel of Figure 2 — that is, $(\nabla b_\gamma)\cdot\mathbf{e}_{\beta'}$ (Elsden & Wright, 2017). In the present simulation the angle between $\mathbf{e}_{\beta'}$ and $\mathbf{e}_\beta$ is quite small ($\theta = 0.09$), so we may approximate the required component as $(\nabla b_\gamma)\cdot\mathbf{e}_\beta$, which is easier to calculate and accurate to leading order in θ.

Simply having a large pressure gradient is not enough to drive a resonant Alfvén wave: it is essential that the variation in time occurs at the required frequency. With this in mind the frequency spectrum of $\partial b_\gamma(\alpha, \beta, 0, t)/\partial\beta$ at $f = f_{wg}$ is the key quantity and is shown as color contours in the fifth panel of Figure 2. The red regions in this panel indicate where the magnetic pressure gradient in β is both large and at the right frequency to favor resonant Alfvén wave excitation.

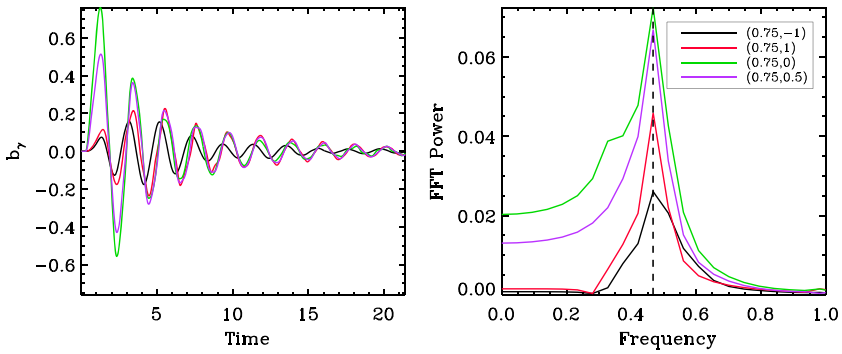

Figure 3. Variation of $b_\gamma(t)$ for several points in the equatorial plane (left) along with the associated frequency spectra (right).

3.3. Resonance Map

The final requirement is that the Alfvén frequency of field lines in regions colored red in the fifth panel of Figure 2 be able to match that of the fast mode. To visualize this Wright and Elsden (2016) introduced the idea of a Resonance Map, which divides the equatorial plane into a Resonant Zone and a Non-Resonant Zone. Focusing on the fundamental Alfvén eigenmode again, recall that $\omega_A(\alpha, \beta, \theta)$ explicitly depends upon the polarization of the Alfvén wave. Choosing a field line and running through $0 < \theta < \pi$ allows the maximum and minimum ω_A for that field line to be determined ($\omega_{\text{Amax}}(\alpha, \beta)$ and $\omega_{\text{Amin}}(\alpha, \beta)$). If $\omega_{wg} = 2\pi f_{wg}$ satisfies $\omega_{\text{Amin}}(\alpha, \beta) < \omega_{wg} < \omega_{\text{Amax}}(\alpha, \beta)$, then there is a polarization (θ) for which the field line may be resonantly excited, $\omega_A(\alpha, \beta, \theta) = \omega_{wg}$, and the field line is said to lie in the Resonant Zone. If this inequality cannot be satisfied, the field line can never be resonant and lies in the Non-Resonant Zone. In the fifth panel of Figure 2 the left-hand line corresponds to field lines where $\omega_{\text{Amin}}(\alpha, \beta) = \omega_{wg}$, the right-hand line to where $\omega_{\text{Amax}}(\alpha, \beta) = \omega_{wg}$, and the region between is the Resonant Zone.

For the simple magnetic geometry adopted in our model $\omega_{\text{Amax}}(\alpha, \beta)$ corresponds to the toroidal frequency, and any field line on the right-hand edge of the Resonant Zone will be resonant if a toroidal polarization is adopted. Conversely, the left-hand boundary will correspond to resonant field lines for a poloidal polarization. The intersection of the Resonant Zone with the red region in the fifth panel of Figure 2 identifies the site where maximum resonant coupling occurs—at dawn. Interestingly, there is smaller peak at dusk (0.82,0.4) but this does not have a strong intersection with the Resonant Zone. Consequently, the fast waveguide mode does not couple as strongly to FLRs at dusk. The dawn FTED peak location and associated polarization are also plotted on the fifth panel of Figure 2. A close inspection shows that the FTED peak is indeed located inside the Resonant Zone. Moreover it is close to the right-hand boundary of the Resonant Zone, which is to be expected as this boundary is associated with a toroidal polarization and the FLR polarization deviates from toroidal by a small amount here ($\theta = 0.09$).

3.4. FLR Evolution

The dawn/dusk asymmetry can also be appreciated from the viewpoint of a driven damped harmonic oscillator. In terms of the plasma displacement in the $\mathbf{e}_{\beta'}$ direction ($\xi_{\beta'}$) the governing equation is (Wright, 1992)

$$\frac{\partial^2 \xi_{\beta'}}{\partial t^2} + \nu \frac{\partial \xi_{\beta'}}{\partial t} - \frac{1}{h_{\beta'} h_\gamma} \frac{V_A^2}{B} \frac{\partial}{\partial \gamma} \left(\frac{h_{\beta'}}{h_{\alpha'} h_\gamma} \frac{\partial}{\partial \gamma} (\xi_{\beta'} h_{\alpha'} B) \right) = \frac{1}{h_\gamma} \frac{V_A^2}{B} \left(-\frac{1}{h_{\beta'}} \frac{\partial (b_\gamma h_\gamma)}{\partial \beta'} \right). \quad (4)$$

Here ν is the coefficient of a small linear drag term ($-\nu\mathbf{u}$) added to the equation governing $\partial\mathbf{u}/\partial t$ to prevent singular behavior developing. The term on the right-hand side is proportional to the magnetic pressure gradient and drives the damped harmonic oscillator on the left-hand side. This can be seen more explicitly by considering an eigenfunction expansion.

The Sturm-Liouville system (equation ((3))) strictly describes ideal eigenfuctions ($\xi_{\beta' n}$) in the absence of dissipation. However, they have the useful property that they form a complete set, so formally we can write a general solution in terms of a sum over these eigenfunctions with appropriate coefficients that depend on t (e.g., as in time-dependent perturbation theory in quantum mechanics),

$$\xi_{\beta'} = \sum_n a_n(t)\xi_{\beta' n}. \tag{5}$$

The eigenfunctions ($\xi_{\beta' n}$) are also orthogonal (Wright & Thompson, 1994)

$$\int \xi_{\beta' n}\xi_{\beta' m} h_{\alpha'} h_{\beta'} h_\gamma \frac{B^2}{V_A^2} \mathrm{d}\gamma = 0, n \neq m. \tag{6}$$

when integrated along the length of the field line. Returning to the third term on the left of equation (4), if $\xi_{\beta'}$ is written as a sum using equation (5), the resulting differential operator acting on the eigenfunctions $\xi_{\beta' n}$ may be substituted for using equation (3) to give

$$-\frac{1}{h_{\beta'} h_\gamma}\frac{V_A^2}{B}\frac{\partial}{\partial\gamma}\left(\frac{h_{\beta'}}{h_{\alpha'} h_\gamma}\frac{\partial}{\partial\gamma}(\xi_{\beta'} h_{\alpha'} B)\right) = \sum_n a_n(t)\omega_{An}^2 \xi_{\beta' n}. \tag{7}$$

Substituting for the remaining $\xi_{\beta'}$ terms in equation (4) using equation (5), it is possible to determine the equation governing any coefficient by multiplying the entire equation by the corresponding eigenfunction and a weighting factor of $h_{\alpha'} h_{\beta'} h_\gamma B^2/V_A^2$ before integrating along the field line and making use of equation (6). The result is an equation for $a_n(t)$ ($n = 1, 2, 3...$),

$$\frac{\mathrm{d}^2 a_n}{\mathrm{d}t^2} + \nu\frac{\mathrm{d}a_n}{\mathrm{d}t} + \omega_{An}^2 a_n = -\frac{\int \xi_{\beta' n} h_{\alpha'} B \frac{\partial(b_\gamma h_\gamma)}{\partial\beta'}\mathrm{d}\gamma}{\int \xi_{\beta' n}^2 h_{\alpha'} h_{\beta'} h_\gamma \frac{B^2}{V_A^2}\mathrm{d}\gamma}. \tag{8}$$

Once the integrals have been performed, the driving term on the right-hand side of equation (8) reduces to $d(t)$—i.e., it is solely a function of time. The magnitude of d will depend upon how well the Alfvén wave eigenfunction ($\xi_{\beta' n}$) and the magnetic pressure gradient ($\propto \partial(b_\gamma h_\gamma)/\partial\beta'$) match up with one another. For example, a fast mode with odd symmetry about the equator and an Alfvén eigenmode with even symmetry would have $d = 0$.

It is fairly easy to see the resonant behavior in the above equation by considering a steady driving term that matches the ideal Alfvén frequency of the rth (resonant) harmonic: $d(t) = d_0 \sin(\omega_{Ar} t)$. The exact solution to equation (8) with boundary conditions $a_r = \mathrm{d}a_r/\mathrm{d}t = 0$ at $t = 0$ is

$$a_r(t) = \frac{\mathrm{d}_0 \exp(-\nu t/2)}{\omega_{Ar}}\left(\frac{\cos(\Omega t)}{\nu} + \frac{\sin(\Omega t)}{2\Omega}\right) - \frac{\mathrm{d}_0}{\omega_{Ar}\nu}\cos(\omega_{Ar} t) \tag{9}$$

where $\Omega = \sqrt{\omega_{Ar}^2 - \nu^2/4}$. In the limit of small dissipation ($\nu \ll \omega_{Ar}$) a series expansion in ν reveals the leading order behavior at early times to be

$$a_r(t) \approx \frac{\mathrm{d}_0}{2\omega_{Ar}^2}\sin(\omega_{Ar} t) - \frac{\mathrm{d}_0}{2\omega_{Ar}} t\cos(\omega_{Ar} t) + \mathcal{O}(\nu). \tag{10}$$

The classic features of a resonant response are present in the second term on the right-hand side: there is secular growth ($\propto t$) at early times and it has a phase lag of $\pi/2$ relative to the driving term (which we assumed was $\mathrm{d}_0 \sin(\omega_{Ar} t)$). At later times the higher-order terms in ν become more important and allow the resonance to saturate with $a_r(t) \approx -(\mathrm{d}_0/\nu\omega_{Ar})\cos(\omega_{Ar} t)$, $t \gg 1/\nu$.

As mentioned previously, the peak FLR amplitudes at dawn and dusk occur at $(\alpha, \beta) = (0.797, -0.714)$ and $(0.728, 0.934)$, respectively. It should be possible to appreciate the preferential FLR excitement at dawn by comparing the driver $\partial b_\gamma/\partial\beta'$ and the response ξ'_β at these two locations. This is done in Figure 4 where we use $\partial b_\gamma/\partial\beta$ and $u_\beta = \partial\xi_\beta/\partial t$ as proxies for these quantities, given that $\theta = 0.09 \ll 1$. The bottom two panels show the pressure gradients that drive the peak FLRs at dawn and dusk. The drift of the fast mode to dusk evidently has the effect of producing slightly larger gradients at dawn compared to dusk. This can be appreciated naively by considering a localized fast mode whose pressure is initially symmetric about noon. The pressure gradient will be zero at noon and switch sign from dawn to dusk—that is, there is a phase change of π of the driver in equation (4).

Consider the structure described above drifting toward dusk (as indicated by the fourth panel of Figure 2) while it oscillates. A field line located on the dawn flank will always remain dawnward of the fast mode pressure

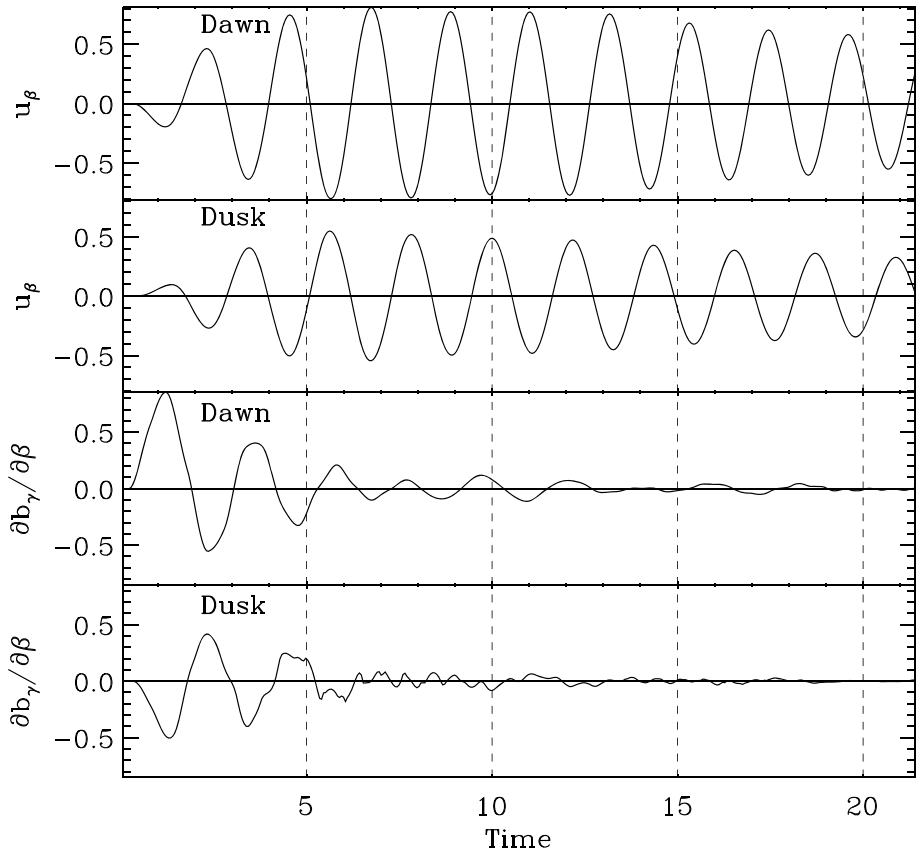

Figure 4. The panels show the temporal variations of various quantities in the equatorial plane at the dawn ($\alpha = 0.797$, $\beta = -0.714$) and dusk ($\alpha = 0.728$, $\beta = 0.934$) FTED peaks. From top to bottom, panel (1) u_β at dawn; (2) u_β at dusk; (3) $\partial b_\gamma/\partial\beta$ at dawn; $\partial b_\gamma/\partial\beta$ at dusk. FTED = Flux Tube Energy Density.

peak so will always experience a pressure gradient with a consistent phase. The same is not true of a field line on the dusk flank: as the peak pressure reaches the field line, the pressure gradient (the driver) drops to zero and thereafter changes phase by π, which could potentially act to decrease the FLR amplitude. The exact details are complicated by factors such as the location of the field lines we consider, the period of the fast mode, the azimuthal extent of the fast mode, and the azimuthal propagation speed. It should also be remembered that the fast mode decays in amplitude as it drives the FLR, so this sets a timescale on which the above effects need to be considered. Nevertheless, these ideas clearly favor coherent FLR driving at dawn compared to dusk. This gives some insight into why the early ($0 < t < 5$) pressure gradients are larger at dawn. Correspondingly, the early u_β response at dusk is around 70% of that at dawn. At later times ($t > 5$) a small coherent pressure gradient persists at dawn, but is completely absent at dusk. Although the dawn driver for this interval is small, it still has a significant effect as it is resonant. At $t = 20$ the dusk FLR amplitude is only 60% of that at dawn.

4. Waveguide Refraction

The simulation results and interpretation presented above rely on the fact that our asymmetric waveguide tends to cause fast mode energy to drift from dawn toward dusk—but why does this occur? A natural way to discuss fast wave propagation is in terms of phase and group velocities. This was exploited in axisymmetric equilibria by Rickard and Wright (1994) who showed how the frequency of a waveguide mode (for given radial and field-aligned harmonics) depended upon the azimuthal wave number, $\omega_{wg}(k_\beta)$. They went on to determine $\omega_{wg}(k_\beta)$ using WKB theory, allowing the phase $(\omega_{wg}(k_\beta)/k_\beta)$ and group $(\partial\omega_{wg}(k_\beta)/\partial k_\beta)$ velocities to be used to interpret their simulation results. This approach can work well in an axisymmetric waveguide ($\partial/\partial\beta = 0$); however, in the waveguide we consider here the asymmetry present prohibits considering a mode with a single value of k_β. Although we cannot use this approach, Wright (1994) showed how ray

tracing could be bounce averaged to provide an alternative derivation of the group velocity. Moreover, the ray tracing approach can be used in waveguides that are not axially symmetric.

4.1. Ray Trajectories

In a similar fashion to a light ray being refracted in a medium with a nonuniform refractive index, we can think of a fast mode ray being refracted by a nonuniform Alfvén speed. Traditionally, the orientation of the ray trajectory is described in terms of angles, which are related to the wavenumbers that a normal mode formulation would favor. The fast mode ray equation is (e.g., Chen, 1998)

$$\frac{\mathrm{d}}{\mathrm{d}s}\left(\frac{1}{V_A}\frac{\mathrm{d}\mathbf{r}}{\mathrm{d}s}\right) = \nabla\left(\frac{1}{V_A}\right). \tag{11}$$

Here V_A may be a function of all three coordinates, s is a parameter (path length) along the ray, and $\mathbf{r}(s)$ is a point on the ray trajectory. Figure 5 illustrates some properties of rays. The top of the schematic shows a wave packet with three wavefronts propagating along a ray path (shown as the solid line with an arrow). As an illustrative example, we focus on rays confined to the equatorial plane and define their orientation in terms of the angle (ϕ) that they make to the α axis. Exploiting the fact that, in the equatorial plane, α and β correspond to Cartesian coordinates we can define

$$\tan\phi = \frac{|\mathrm{d}\alpha|}{\mathrm{d}\beta} = \frac{|\mathrm{d}\alpha/\mathrm{d}t|}{\mathrm{d}\beta/\mathrm{d}t}. \tag{12}$$

If the Alfvén speed varies along a given wavefront, then one side of the wavefront will travel more quickly than the other and the ray path will turn, ϕ will change, and the ray trajectory will bend. This process of refraction is described by equation (11). Evidently it operates when $\nabla V_A \neq 0$, and the nature of the ray path is sensitive to the details of V_A. In the equilibrium described in section 2.2 there is a tendency to have V_A decrease from dawn to dusk. Imagine how this affects a ray launched earthward from the magnetopause directly along the α axis, that is, initially $\phi = 0$: The dawnside of the wavefront propagates faster than the duskside, so the ray path turns toward dusk and subsequently propagates in that direction. The ray is also propagating in α, and for the equilibria used here is likely to reach an inner boundary (the plasmapause) where it is reflected. This type of trajectory is shown over a full bounce in the lower part of the schematic in Figure 5. Also indicated for this ray are ϕ_n and ϕ_{n+1} (the magnetopause values of ϕ for the n and $n+1$ reflections) along with $\Delta\beta$, the distance moved over one full bounce. If the radial variation in V_A is increased the wave refraction can be strong enough to introduce a turning point where the radial motion is reversed. If the time of the magnetopause encounters are known (call these t_n and t_{n+1}), Wright (1994) showed that the bounce-averaged β component of the group velocity is

$$\overline{V}_{g\beta} \equiv \frac{\Delta\beta}{t_{n+1} - t_n}. \tag{13}$$

Since the time taken for a bounce is found from integrating

$$\frac{\mathrm{d}t}{\mathrm{d}s} = \frac{1}{V_A}, \tag{14}$$

ray tracing allows us to deduce the speed at which fast mode energy will propagate azimuthally in an asymmetric waveguide when it is not appropriate to consider modes proportional to $\exp i(\omega t - k_\beta \beta)$.

4.2. Wavepacket Refraction and Propagation

For the equilibirium adopted in our simulations, the ray tends to bounce back and forth between the magnetopause and plasmapause, while shuffling from dawn to dusk. Elsden and Wright (2018) noted that the ray tracing behavior could be revealed quite directly in their simulations by adjusting the driving condition by reducing τ_d so that the magnetopause is effectively given a quick push. This has the effect of launching a localized fast mode wave packet into the magnetosphere and is depicted as the three snapshots of $|b_\gamma(\alpha, \beta, 0, t)|$ in the color panels of Figure 5 for $\tau_d = \pi/30$. (Other parameters are unchanged.) A crude appreciation of the ray trajectory for this wave packet may be envisaged by considering the location of the maximum value of $|b_\gamma|$ at any time, $(\alpha(t), \beta(t))$. In each snapshot the dot represents the location of the maximum at that time, and the line shows the locus of the maximum at previous times.

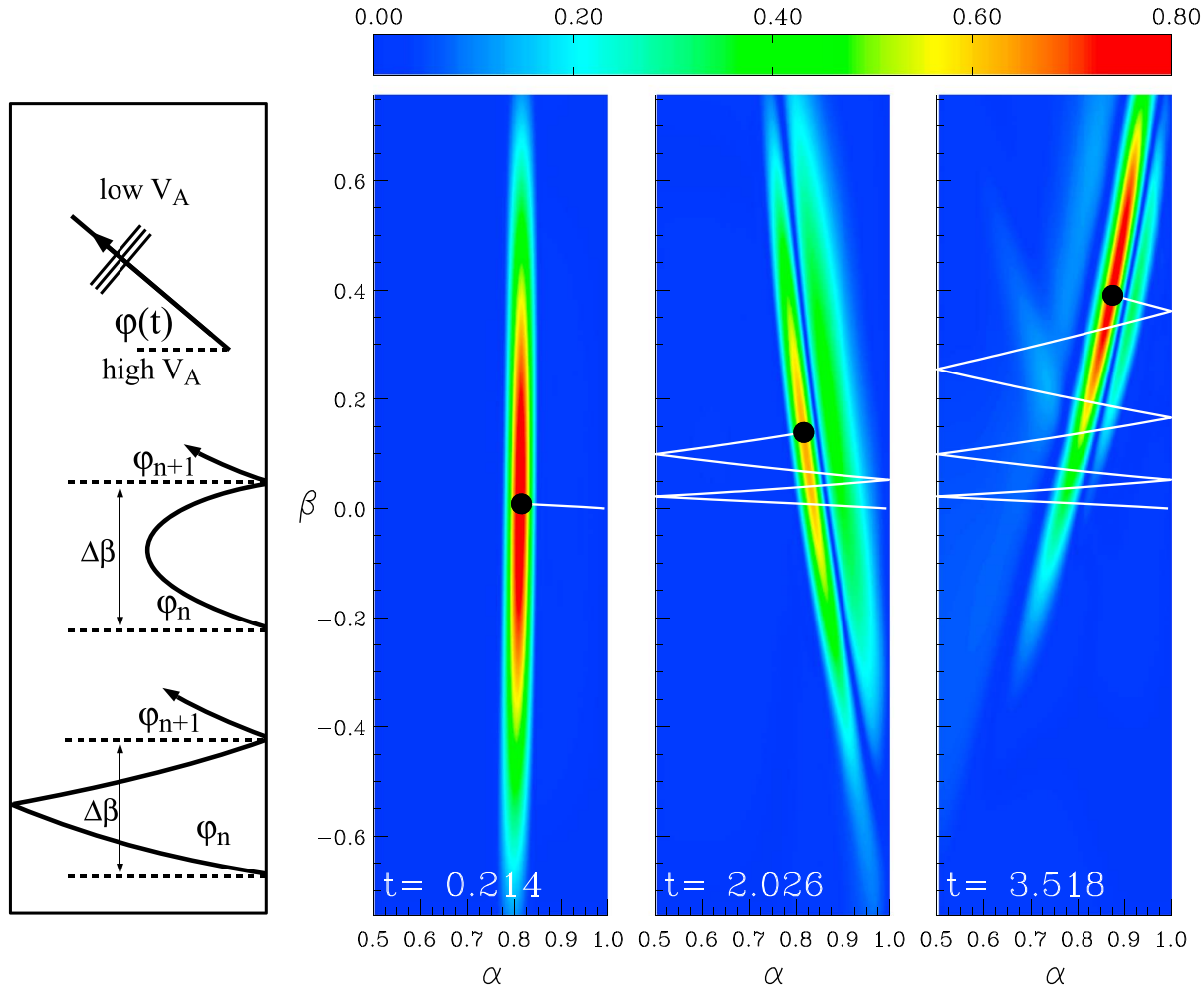

Figure 5. Schematic: Ray trajectories and their orientation (ϕ) in the equatorial plane. Color panels: snapshots of $|b_\gamma(\alpha, \beta, t)|$ in the equatorial plane. The dot represents the current location of the maximum, and the line is its locus/path at earlier times. (The duration of driver is $\tau_d = \pi/30$. See section 2.1 for further details.).

The $t = 0.214$ panel in Figure 5 shows the wavefront traveling to the left shortly after it has been launched. By $t = 2.026$ it has been reflected twice off the left-hand boundary and is travelling to the right. At this stage it is already evident that the higher V_A at dawn ($\beta < 0$) has caused that part of the wavefront to run ahead and turn the orientation so that there is now a noticeable motion toward dusk. This becomes increasingly apparent at later times as shown by the right-hand panel of Figure 5.

To study the properties of the ray trajectories in more detail, we reproduce the path found in Figure 5 as the middle panel of Figure 6. This path is characterized by being launched at $t = 0$ with its center at $(\alpha, \beta) = (1, 0)$ and propagating antiparallel to the α axis—that is, $\phi(t = 0) = 0$. Similar simulations to that shown in Figure 5 were performed with a modified magnetopause driver that could launch the wavefront from (1,0) but with an arbitrary initial inclination $\phi(0)$. One such run used $\phi(0) = 0.2$, and the corresponding ray is shown as the right-hand panel of Figure 6. The local group velocity of the wavepacket in the β direction is

$$V_{g\beta} = V_A \sin\phi(t), \tag{15}$$

so it is traveling toward dusk from the start. (Note that the modulus signs in equation (12) mean duskward/dawnward propagation corresponds to ϕ being positive/negative, respectively.) In contrast, the first panel of Figure 6 shows results for $\phi(0) = -0.2$, so the wavepacket is initially traveling toward dawn. In this case refraction first reduces the speed of dawnward travel to zero at $\beta \approx -0.22$, and thereafter, duskward propagation is maintained. (The portion of the path colored red corresponds to dawnward propagation.)

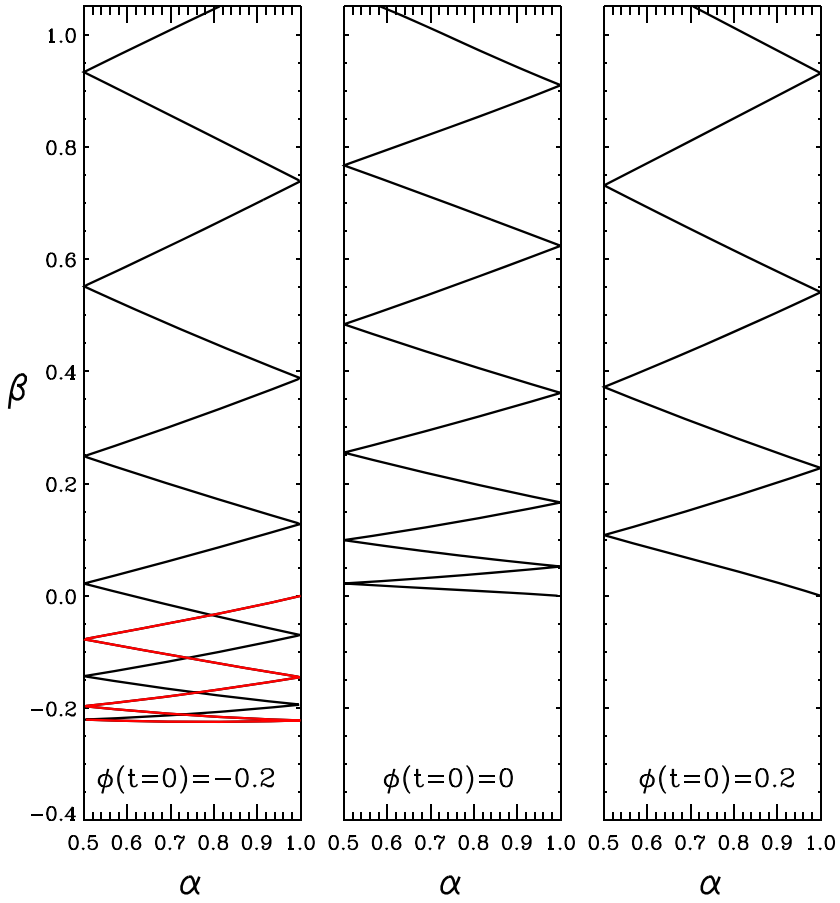

Figure 6. Ray trajectories (based upon tracking $|b_\gamma|$ as in Figure 5) for three simulations with launch angles $\phi(t = 0) = -0.2, 0.0$, and 0.2. All rays start from $(\alpha, \beta) = (1, 0)$ at $t = 0$. The section of raypath colored red corresponds to dawnward propagation, while black denotes duskward propagation.

The location of the fast mode energy in the fourth panel of Figure 2 over $0.0 < \beta < 1.0$ starting at $t = 5$ can also be appreciated using ray trajectories. The magnetopause driver is symmetric about noon, and a Fourier decomposition in terms of wavenumber k_β, or equivalently ϕ, will have maximum power in a peak centered on $k_\beta = 0$, corresponding to $\phi = 0$. If most of the initial power is in rays with $\phi \approx 0$ launched from $(\alpha, \beta) = (1.0, 0.0)$ around $t \approx 0$, we can estimate where they will be at $t = 5$ from the $\beta(t = 5)$ curve in the bottom panel of Figure 7 for the $\phi(0) = 0$ ray. This suggests that $\beta \approx 0.7$. An alternative estimate was found by numerical integration of the ray equation (11) using the fourth-order Runge-Kutta scheme, which yielded $\beta = 0.71$ at $t = 5.0$. Both these values are in good agreement with observed location in the simulation shown in the fourth panel of Figure 2.

Information about the speed of propagation along the paths shown in Figure 6 can be gleaned by plotting the α and β values as functions of time—as is done in Figure 7. The top three panels show $\alpha(t)$ for an initial ϕ of −0.2, 0.0, and 0.2. The bouncing nature of the ray between $\alpha = 0.5$ and 1.0 is evident. The bottom panel shows $\beta(t)$ for the three wave packet simulations. The section colored red has $d\beta/dt < 0$, so corresponds to the initial dawnward propagation noted in Figure 6 for $\phi(0) = -0.2$. By calculating $d\alpha/dt$ and $d\beta/dt$ for the curves in Figure 7 the ratio may be used to determine $\phi(t)$ using equation (12), which then allows the local group velocity of the wave packet in the β direction ($V_{g\beta}$) to be found from equation (15). The local $V_{g\beta}$ of the wave packet can also be found directly from the slope of the $\beta(t)$ curve shown in Figure 7.

4.3. Bounce-Averaged Propagation

For the purposes of describing the global propagation of fast mode energy, it is useful to form $\overline{V}_{g\beta}$—the bounce-averaged β component of the group velocity, as defined in equation (13). We shall illustrate how to do this for the $\phi(0) = 0$ simulation: In Figure 7 the red dots indicate the values of α, β, and t for which the ray is at

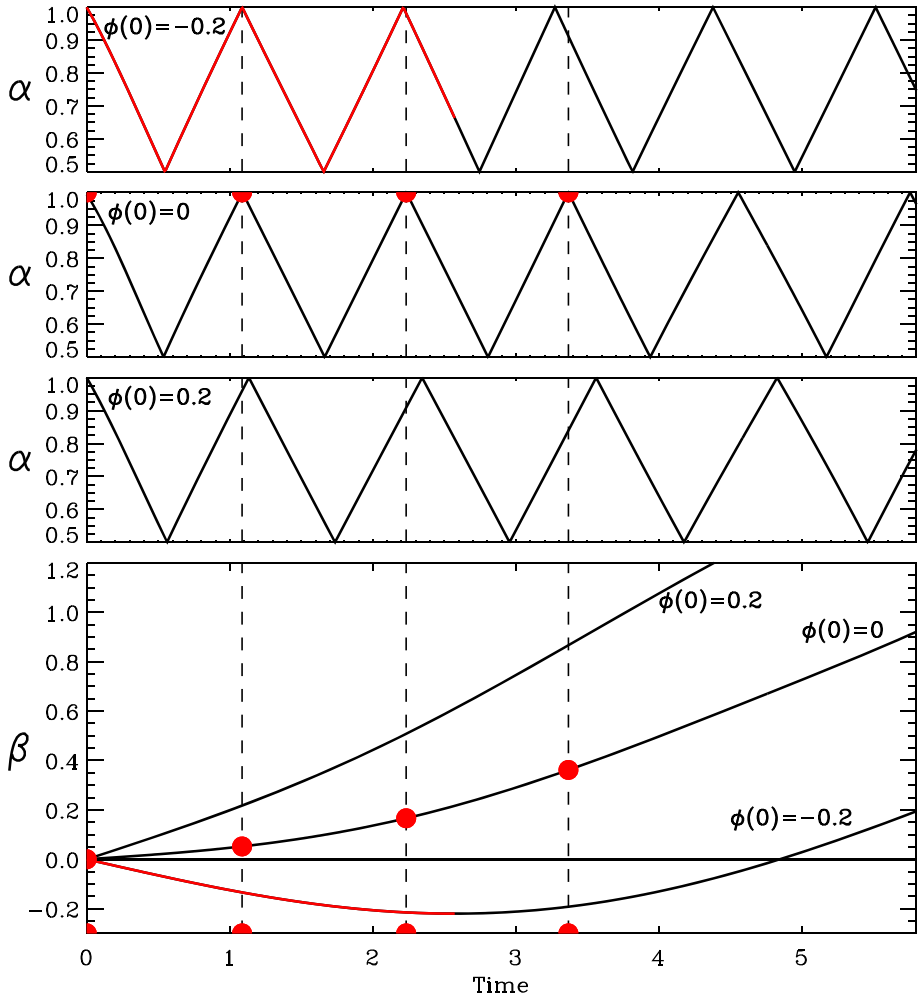

Figure 7. Variation of α and β with t for the three rays shown in Figure 6. Top three panels: $\alpha(t)$ for the simulations with $\phi(0) = -0.2$, 0.0, and 0.2. Bottom panel: $\beta(t)$. The portion colored red corresponds to initial dawnward propagation. The vertical lines identify times for which the $\phi(0) = 0$ ray is at the magnetopause ($\alpha = 1$). The red dots identify the corresponding values of α, β, and t.

the magnetopause. The β values at these times allow $\Delta\beta$ to be determined. Also, ϕ_n is calculated as described above, and the bounce-averaged value estimated as $\overline{\phi} = (\phi_{n+1} + \phi_n)/2$. On employing equations (12) and (13) we arrive at a pair of bounce-averaged values, $\overline{V}_{g\beta}$ and $\overline{\phi}$.

Calculating values for $\overline{V}_{g\beta}$ and $\overline{\phi}$ from 3-D time-dependent simulations is computationally far more expensive than solving equation (11) for the ray trajectory directly. For this reason further evaluation of $\overline{V}_{g\beta}$ and $\overline{\phi}$ is based upon numerical solutions to (11). The bounces used in these calculations were distributed throughout the waveguide, and the results are shown as the black dots in Figure 8. The trend is as expected: if $\overline{\phi} \approx 0$ the ray is propagating in α, and $\overline{V}_{g\beta} \approx 0$. As $\overline{\phi}$ increases/decreases, $\overline{V}_{g\beta}$ increases/decreases. Also included are four red dots, which resulted from the $\phi(0) = 0$ simulation described in Figure 7. As the red and black dots show consistency, this validates the use of the ray equation for describing the wave packet simulations. Moreover, Elsden and Wright (2018) showed how the wave packet simulation bounce period could accurately estimate the fundamental waveguide mode frequency, which we can now also evaluate using the ray equation.

In the case of a waveguide with uniform V_A the local wave packet group velocity ($V_A \sin\phi$, equation (15) would be the same as the bounce-averaged value. With this in mind we evaluated the spatial average of V_A in the equatorial plane where most of the rays used to calculate Figure 8 were located ($0.5 < \alpha < 1.0$, $-1.0 < \beta < 1.0$) to be $\overline{V}_A = 0.915$, and have included the line $\overline{V}_A \sin\overline{\phi}$ in Figure 8 as a crude estimate of the general relation between $\overline{V}_{g\beta}$ and $\overline{\phi}$. The general trend is evident, as is the scatter of points around it which is to be expected.

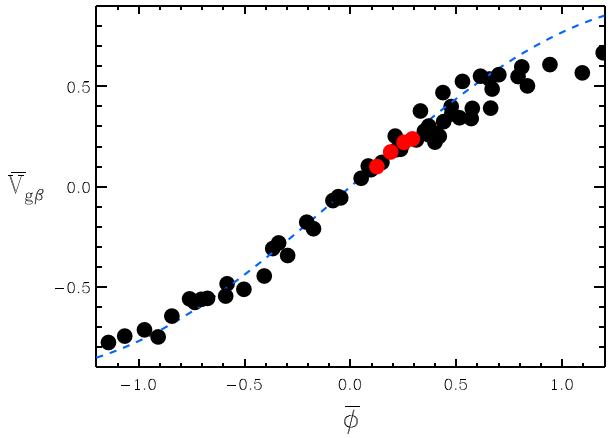

Figure 8. Bounce-averaged group velocity versus bounce-averaged ϕ. The black dots are based upon solutions to the ray trajectory equation, the red dots are from the wave packet simulation in Figure 5. The dashed line is $\overline{V}_A \sin \overline{\phi}$, $\overline{V}_A$ being the mean V_A.

5. Discussion and Conclusion

We have presented simulations of ULF waves in an asymmetric waveguide model of magnetosphere. A realistic variation of toroidal Alfvén frequency requires an equilibrium model in which V_A is larger at dawn compared to dusk. When this system is driven by magnetopause pressure perturbations that are symmetric about noon, the resulting fast mode waves that are produced in the magnetosphere are refracted in a manner that causes asymmetries to develop: specifically, the fast waves acquire an eastward azimuthal group velocity associated with refraction. This interpretation has been supported by solving the fast ray trajectory equation.

The asymmetric fast mode produces pressure gradients suitable for driving FLRs at both dawn and dusk. However, those at dawn are larger and more coherent than those at dusk. Crucially, the Resonant Zone (the region where it is possible for the Alfvén frequency to match the fast mode frequency) shows a strong overlap with the region where the coherent pressure gradients exist at dawn, which is not the case at dusk. For these reasons FLRs are driven preferentially in our simulation on the dawn flank compared to the dusk flank.

The results of the simulations are in good agreement with spacecraft observations of the dawn/dusk asymmetry of Pc5 Alfvén waves (FLRs) in the outer magnetosphere (period = 150–600 s). Waves on the dawnside with a strong toroidal component that are consistent with the second and third panels of Figure 2 are well documented in statistical studies of ground and satellite data as mentioned in section 1. The simulation results are also quantitatively consistent with satellite observations. For example, Takahashi et al. (2015) indicate that the median amplitude of the toroidal velocity component of fundamental Alfvén waves at $L = 10–12$ is 30% higher at dawn than at dusk. This matches well with the numerical results shown in the first and second panels of Figure 4.

In some observational studies, ULF wave activity is defined in terms of *occurrence* of narrowband oscillations (e.g., Baker et al., 2003; Takahashi et al., 2015). We argue that the occurrence probability is roughly equivalent to the spectral intensity (or amplitude) of the waves. Occurrence of a wave event is identified when a spectral peak rises above the background (e.g., Takahashi et al., 2015). If the background remains the same on each flank, the occurrence probability of a wave increases when its amplitude increases. The simulation results thus explains observational results that used the occurrence probability as a parameter to describe Pc5 activity.

The simulation indicates that the amplitude of both fast mode waves and Alfvén waves exhibit dawn/dusk asymmetry and that an interesting propagation, refraction, and coupling process between these wave modes needs to be taken into account to explain the asymmetry. Simulations can provide valuable information about the spatial variation of fast mode waves, which can be challenging to measure in the real magnetosphere. Such measurements inevitably require statistical analysis of spacecraft data, but in doing so, one realizes that magnetically compressional ULF waves in the outer magnetosphere result both from instabilities in the magnetosphere and from propagation of disturbances from the solar wind as the fast mode (Takahashi et al., 2016). Because the fast mode waves often have small amplitudes (Hartinger et al., 2013), it is difficult to separate them out from magnetic field time series that contains contribution from both wave types. While the spatial

distribution of the mass density and amplitudes of the toroidal component of Alfvén waves can be obtained relatively easily, the behavior of fast mode waves can be studied most easily using numerical simulations.

Acknowledgments
A. N. W. was partially funded by STFC (ST/N000609/1) and the Leverhulme Trust (RPG-2016-071). T. E. was funded by the Leverhulme Trust (RPG-2016-071). K. T. was supported by NASA grant NNX17AD34G. Data used to produce the simulation plots can be accessed at https://figshare.com/authors/Tom_Elsden/4743264. The THEMIS data used in this study are publicly available from the THEMIS mission home page maintained by the Space Science Laboratory, University of California, Berkeley (http://themis.ssl.berkeley.edu).

References

Allan, W., White, S. P., & Poulter, E. M. (1986). Impulse-excited hydromagnetic cavity and field-line resonances in the magnetosphere. *Planetary and Space Science*, *34*, 371.
Baker, G., Donovan, E. F., & Jackel, B. J. (2003). A comprehensive survey of auroral latitude Pc5 pulsation characteristics. *Journal of Geophysical Research*, *108*(A8), 1384. https://doi.org/10.1029/2002JA009801
Chen, H.-W. (1998). Three-dimensional geometrical ray theory and modelling of transmitted seismic energy of data from the Nevada Test Site. *Geophysical Journal International*, *133*, 366–378.
Chen, L., & Hasegawa, A. (1974). A theory of long-period magnetic pulsations: 1. Steady state excitation of field line resonance. *Journal of Geophysical Research*, *79*, 1024–1032. https://doi.org/10.1029/JA079i007p01024
Claudepierre, S. G., Hudson, M. K., Lotko, W., Lyon, J. G., & Denton, R. E. (2010). Solar wind driving of magnetospheric ULF waves: Field line resonances driven by dynamic pressure fluctuations. *Journal of Geophysical Research*, *115*, A11202. https://doi.org/10.1029/2010JA015399
de Moura, C. A., & Kubrusly, C. S. (2013). *The Courant–Friedrichs–Lewy condition*. New York: Springer. https://doi.org/10.1007/978-0-8176-8394-8
Degeling, A. W., Rankin, R., Kabin, K., Rae, I. J., & Fenrich, F. R. (2010). Modeling ULF waves in a compressed dipole magnetic field. *Journal of Geophysical Research*, *115*, A10212. https://doi.org/10.1029/2010JA015410
Ellington, S. M., Moldwin, M. B., & Liemohn, M. W. (2016). Local time asymmetries and toroidal field line resonances: Global magnetospheric modeling in SWMF. *Journal of Geophysical Research: Space Physics*, *121*, 2033–2045. https://doi.org/10.1002/2015JA021920
Elsden, T., & Wright, A. N. (2017). The theoretical foundation of 3-D Alfvén resonances: Time-dependent solutions. *Journal of Geophysical Research: Space Physics*, *122*, 3247–3261. https://doi.org/10.1002/2016JA023811
Elsden, T., & Wright, A. N. (2018). The broadband excitation of 3D Alfvén resonances in a MHD waveguide. *Journal of Geophysical Research: Space Physics*, *123*, 530–547. https://doi.org/10.1002/2017JA025018
Fujita, S., & Itonaga, M. (2003). A plasmaspheric cavity resonance in a longitudinally nonuniform plasmasphere. *Earth Planets and Space*, *55*(4), 219–222. https://doi.org/10.1186/Bf03351751
Gallagher, D. L., Craven, P. D., & Comfort, R. H (2000). Global core plasma model. *Journal of Geophysical Research*, *105*(A8), 18819–18833. https://doi.org/10.1029/1999ja000241
Gupta, J. C. (1975). Long-period Pc5 pulsations. *Planetary and Space Science*, *23*, 733–750. https://doi.org/10.1016/0032-0633(75)90012-4
Hartinger, M. D., Angelopoulos, V., Moldwin, M. B., Takahashi, K., & Clausen, L. B. N (2013). Statistical study of global modes outside the plasmasphere. *Journal of Geophysical Research: Space Physics*, *118*(2), 804–822. https://doi.org/10.1002/jgra.50140
Kivelson, M. G., & Southwood, D. J. (1986). Coupling of global magnetospheric MHD eigenmodes to field line resonances. *Journal of Geophysical Research*, *91*, 4345.
Kokubun, S. (2013). ULF waves in the outer magnetosphere: Geotail observation 1 transverse waves, Earth. *Planets and Space*, *65*(5), 411–433. https://doi.org/10.5047/eps.2012.12.013
Lee, D. H., & Lysak, R. L. (1989). Magnetospheric ULF wave coupling in the dipole model: The impulsive excitation. *Journal of Geophysical Research*, *94*, 17097.
Lee, L. C., & Olson, J. V (1980). Kelvin–Helmholtz instability and the variation of geomagnetic pulsation activity. *Geophysical Research Letters*, *7*(10), 777–780. https://doi.org/10.1029/GL007i010p00777
Mann, I. R., Wright, A. N., & Cally, P. S. (1995). Coupling of magnetospheric cavity modes to field line resonances: A study of resonance widths. *Journal of Geophysical Research*, *100*, 19441. https://doi.org/10.1029/95JA00820
Nosé, M., Iyemori, T., Sugiura, M., & Slavin, J. A (1995). A strong dawn/dusk asymmetry in Pc5 pulsation occurrence observed by the DE-1 satellite. *Geophysical Research Letters*, *22*(15), 2053–2056. https://doi.org/10.1029/95gl01794
Nosé, M., Oimatsu, S., Keika, K., Kletzing, C. A., Kurth, W. S., De Pascuale, S., et al. (2015). Formation of the oxygen torus in the inner magnetosphere: Van Allen Probes observations. *Journal of Geophysical Research: Space Physics*, *120*, 1182–1196. https://doi.org/10.1002/2014JA020593
Rickard, G. J., & Wright, A. N. (1994). Alfvén resonance excitation and fast wave propagation in magnetospheric waveguides. *Journal of Geophysical Research*, *99*, 13455. https://doi.org/10.1029/94JA00674
Sandhu, J. K., Yeoman, T. K., James, M., Rae, I. J., & Fear, R. C. (2018). Variations of high-latitude geomagnetic pulsation frequencies: A comparison of time-of-flight estimates and IMAGE magnetometer observations. *Journal of Geophysical Research: Space Physics*, *123*, 567–586. https://doi.org/10.1002/2017JA024434
Sandhu, J. K., Yeoman, T. K., Rae, I. J., Fear, R. C., & Dandouras, I. (2017). The dependence of magnetospheric plasma mass loading on geomagnetic activity using Cluster. *Journal of Geophysical Research: Space Physics*, *122*, 9371. https://doi.org/10.1002/2017ja024171
Singer, H. J., Southwood, D. J., Walker, R. J., & Kivelson, M. G. (1981). Alfvén wave resonances in a realistic magnetospheric magnetic field geometry. *Journal of Geophysical Research*, *86*, 4589.
Southwood, D. J. (1974). Some features of field line resonances in the magnetosphere. *Planetary and Space Science*, *22*, 483–491. https://doi.org/10.1016/0032-0633(74)90078-6
Takahashi, K., Hartinger, M. D., Angelopoulos, V., & Glassmeier, K.-H. (2015). A statistical study of fundamental toroidal mode standing Alfvén waves using THEMIS ion bulk velocity data. *Journal of Geophysical Research: Space Physics*, *120*, 6474–6495. https://doi.org/10.1002/2015ja021207
Takahashi, K., Lee, D.-H., Merkin, V. G., Lyon, J. G., & Hartinger, M. D. (2016). On the origin of the dawn-dusk asymmetry of toroidal Pc5 waves. *Journal of Geophysical Research: Space Physics*, *121*, 9632–9650. https://doi.org/10.1002/2016JA023009
Takahashi, K., Ohtani, S., Denton, R. E., Hughes, W. J., & Anderson, R. R. (2008). Ion composition in the plasma trough and plasma plume derived from a combined release and radiation effects satellite magnetoseismic study. *Journal of Geophysical Research*, *113*, A12203. https://doi.org/10.1029/2008JA013248
Wright, A. N. (1992). Asymptotic and time-dependent solutions of magnetic pulsations in realistic magnetic field geometries. *Journal of Geophysical Research*, *97*, 6439. https://doi.org/10.1029/91JA02666
Wright, A. N. (1994). Dispersion and wave coupling in inhomogeneous MHD waveguides. *Journal of Geophysical Research*, *99*, 159–167. https://doi.org/10.1029/93JA02206
Wright, A. N., & Elsden, T. (2016). The theoretical foundation of 3D Alfvén resonances: Normal modes. *Astrophysical Journal*, *833*, 230. https://doi.org/10.3847/1538-4357/833/2/230
Wright, A. N., & Thompson, M. J. (1994). Analytical treatment of Alfvén resonances and singularities in nonuniform magnetoplasmas. *Physics of Plasmas*, *1*, 691. https://doi.org/10.1063/1.870815